Journal of Materials Chemistry C

ROYAL SOCIETY OF CHEMISTRY

PAPER

View Article Online
View Journal | View Issue



Cite this: J. Mater. Chem. C, 2021, 9, 4643

# Optical pressure sensing in vacuum and high-pressure ranges using lanthanide-based luminescent thermometer–manometer†

Marcin Runowski, *[ab] Przemysław Woźny [a] and Inocencio R. Martín [b]

Received 12th February 2021,
Accepted 5th March 2021

DOI: 10.1039/d1tc00709b

rsc.li/materials-c

Pressure is a fundamental physical parameter, so its monitoring is crucial for various industrial and scientific purposes. However, the available optical sensors allow monitoring in either low pressure or high pressure ranges. In this work, different concepts of pressure sensing are combined, and the first luminescent pressure sensor working within 9-orders of magnitude (from $10^{-4}$ to $10^{5}$ bar) is developed, allowing both low (vacuum) and high pressure sensing. This sensor is based on the inorganic, upconverting material ($YPO_4$:$Yb^{3+}$–$Er^{3+}$) emitting in the visible and near-infrared (NIR) ranges. For vacuum detection, the recently discovered sensing method is applied, which is based on the conversion of a luminescent thermometer into the pressure sensor. This is because of the effect of light-to-heat conversion, which is greatly enhanced under vacuum conditions, and manifested as a change in the intensity ratio of $Er^{3+}$ thermally-coupled bands (525/550 nm). Whereas for high-pressure sensing, the emission line shift of $Er^{3+}$ (induced by materials compression), located in the NIR spectral range, is used.



## Introduction

Pressure and temperature are crucial parameters in most of the scientific research and industrial processes.[1–9] That is why, their rapid, accurate and contactless determination has attracted more and more attention from the researchers.[3–7,10,11] For non-contact determinations of pressure and temperature, optical methods based on the luminescence of lanthanides, d-block metal ions and organic complexes are commonly applied.[3–7,10–14]

Lanthanide (Ln) ions have many favourable spectroscopic properties, such as narrow emission lines, long luminescence lifetimes, broad range multicolour emission, large Stokes shifts, *etc.*, which are related to their 4f–4f electronic transitions.[3–7,15–18] Many inorganic materials doped with $Ln^{2+/3+}$ ions have well-defined temperature and pressure responses, so they can work as luminescent thermometers and manometers.[3–7,10–13] For temperature sensing, the materials containing $Er^{3+}$, $Tm^{3+}$ and $Nd^{3+}$ are predominantly used as luminescent thermometers, due to the presence of thermally-coupled levels (TCLs), separated by a small energy difference ($\approx$50–2000 $cm^{-1}$), hence their emission follows Boltzmann type distribution.[3,4,6,7,10–13,19–22] For high-pressure sensing, usually $Sm^{2+}$ or $Eu^{2+}$ ions embedded in inorganic matrices are used, because they have either narrow emission lines or their emission characteristics are very sensitive to pressure changes, respectively.[23–26] Such materials are an alternative to the well-established and commonly used ruby-based ($Al_2O_3$:$Cr^{3+}$) fluorescent sensor, whose emission, unfortunately, is highly temperature-dependent.[27–29] Whereas for low-pressure, *i.e.*, vacuum sensing, either the organic complexes (dyes) exhibiting oxygen-dependent emission quenching or the inorganic materials exhibiting a pressure-modulated light-to-heat conversion phenomenon (heating–cooling processes monitored *via* luminescence thermometry) are used.[10,11,30,31] However, the oxygen-sensitive organic dyes allow sensing in a very limited pressure range, typically from $\approx$0.05 to 2 bar.[31]

Considering temperature, currently there are various approaches in luminescence thermometry, allowing the development of micron-sized and nano-sized optical thermometers, operating in a broad temperature range, from cryogenic to high-temperatures (above 1000 K).[6,12,13,19–22,32–34] They usually use a band intensity ratio of two thermalized levels or changes in luminescence lifetimes for temperature determination.[6,12,13,20,32–38] Whereas in the case of optical pressure sensors, they work either in the vacuum range or in the high-pressure range.[3–5,7,10,11,36] This is because of their totally different operating principles, namely sensors working in the high-pressure range are based on materials compression, leading to changes in spectroscopic properties of the optically active ions, *e.g.*, line shift, changes in band intensity ratios, emission line width or luminescence lifetimes.[2–5,7,36] Whereas luminescent sensors

[a] Adam Mickiewicz University, Faculty of Chemistry, Uniwersytetu Poznańskiego 8, 61-614 Poznań, Poland. E-mail: runowski@amu.edu.pl
[b] Departamento de Física, Instituto de Materiales y Nanotecnología (IMN), Universidad de La Laguna, Apdo. Correos 456, E-38200 San Cristóbal de La Laguna, Santa Cruz de Tenerife, Spain

† Electronic supplementary information (ESI) available. See DOI: 10.1039/d1tc00709b

working in the vacuum range (below 1 bar) are based predominantly on the changes in the concentration of the surrounding gas molecules, resulting either in the mentioned luminescence quenching (variations of emission intensity) or elevation of the local temperature (the recently discovered method allows the conversion of luminescent thermometers/heaters into vacuum sensors).[10,11,30,31] The last approach, utilizes the effect of laser-induced heating of the materials, enhanced under vacuum conditions.[10,11]

Here we show, for the first time how to combine two different approaches of pressure sensing, *i.e.*, high-pressure materials compression and vacuum-enhanced light-to-heat conversion, and develop the first multi-range optical pressure sensor (see Scheme 1). The developed sensor can operate in the very broad pressure range, from vacuum ($10^{-4}$ bar) up to high-pressure range ($10^{5}$ bar). The luminescent probe is an upconverting material based on inorganic phosphate doped with ytterbium(III) and erbium(III) ions, showing a well-defined thermal and pressure responses, and resistance to treatment under extreme conditions.

## Results and discussion

### Characteristics of the pressure sensor material

The luminescent low (vacuum) and high pressure sensor used in this work is based on $YPO_4$ doped with 15 mol% of $Yb^{3+}$ and 2 mol% of $Er^{3+}$ micron-sized ($\approx$0.5–1 μm) inorganic particles, with a relatively high phonon energy of around $\approx$1100 $cm^{-1}$,[7] crystallizing as tetragonal $YPO_4$, in the $I4_1/amd$ space group (see Fig. S1–S4 that confirm the structure, morphology, and elemental composition of the sensor material, ESI†). The material studied is stable under high-pressure conditions, preserving its tetragonal structure up to ~14 GPa, with a bulk modulus ($B_0$) of ~186(5) GPa.[7,39] The synthesized material is optically active, *i.e.*, it can generate a two-photon upconversion (UC) luminescence, namely the anti-Stokes emission of $Er^{3+}$ under near-infrared (NIR) laser irradiation ($\approx$975 nm), which is commonly observed in various inorganic materials doped with $Yb^{3+}$–$Er^{3+}$ ions. In such a system, $Yb^{3+}$ ("light harvesting ions") effectively absorb the incident NIR laser radiation, and transfer it to the neighbouring $Er^{3+}$ ions (emitters), mostly *via* energy transfer UC processes (see the energy level diagram in Scheme 1b).[4,10,35]

### Low pressure (vacuum) sensing

In order to calibrate the optical response of the developed upconverting vacuum sensor $YPO_4$:$Yb^{3+}$–$Er^{3+}$, we have measured a series of UC emission spectra as a function of temperature ($\approx$300–850 K), using a continuous wave (CW) 975 nm NIR laser (2 W $mm^{-2}$). The normalized spectra presented in Fig. 1a, clearly show temperature dependence of the thermalized bands of $Er^{3+}$, corresponding to the radiative transitions $^2H_{11/2} \rightarrow {}^4I_{15/2}$ ($\approx$525 nm) and $^4S_{3/2} \rightarrow {}^4I_{15/2}$ ($\approx$550 nm). Based on the recorded spectra, we have determined the band intensity ratio of 525/550 nm, integrating the area under the mentioned bands. The determined values are plotted in Fig. 1b as a function of temperature, showing an almost linear dependence, which is typical of $Er^{3+}$ TCLs $^2H_{11/2}$ and $^4S_{3/2}$. Because these energy levels of $Er^{3+}$ are thermally coupled, with $\Delta E \approx 866 \pm 4$ $cm^{-1}$ (value determined from the spectra), they follow Boltzmann type

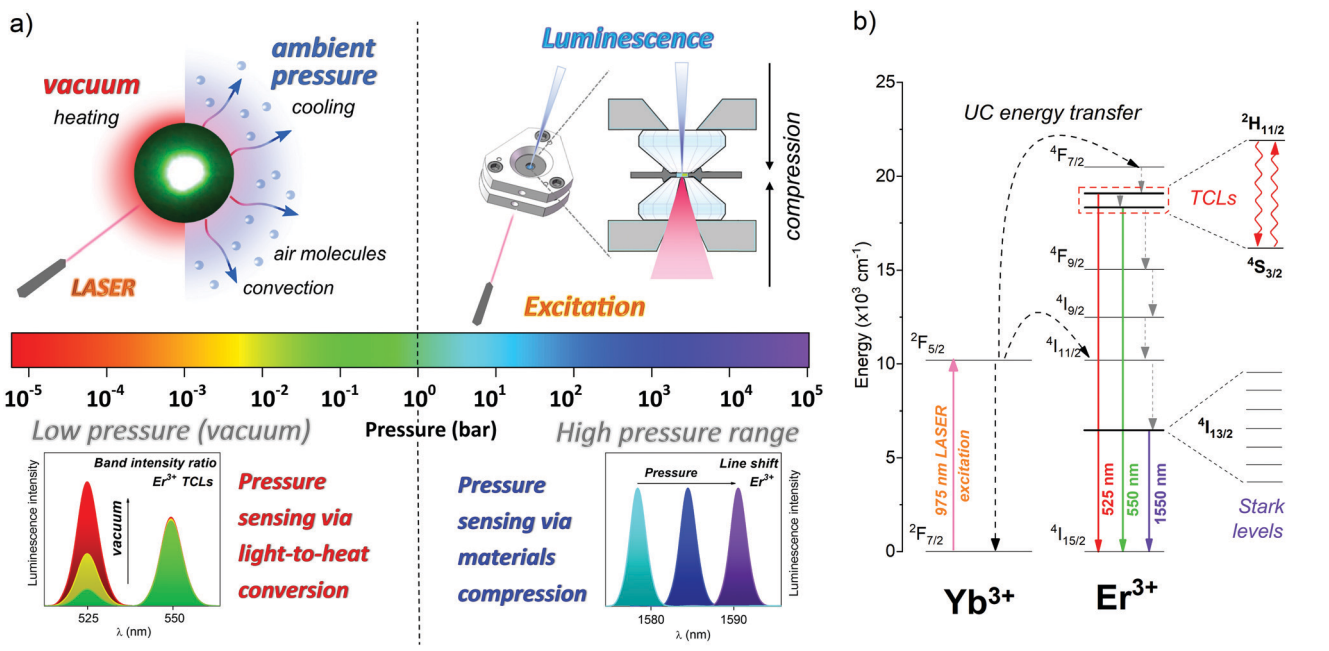


Scheme 1 (a) Two different concepts of pressure sensing combined in a single, $Er^{3+}$-doped luminescent material, working as a multi-range pressure sensor; (left) low pressure, *i.e.*, vacuum sensing *via* light-to-heat conversion, and (right) high pressure sensing *via* materials compression. (b) Energy level diagram showing the main radiative and non-radiative processes taking place in the investigated $Yb^{3+}$–$Er^{3+}$ system, focusing on $Er^{3+}$ TCLs $^2H_{11/2}$ and $^4S_{3/2}$ (for vacuum sensing) and Stark sublevels, *i.e.*, crystal field components of the $^4I_{13/2} \rightarrow {}^4I_{15/2}$ transition (for high-pressure sensing).

 

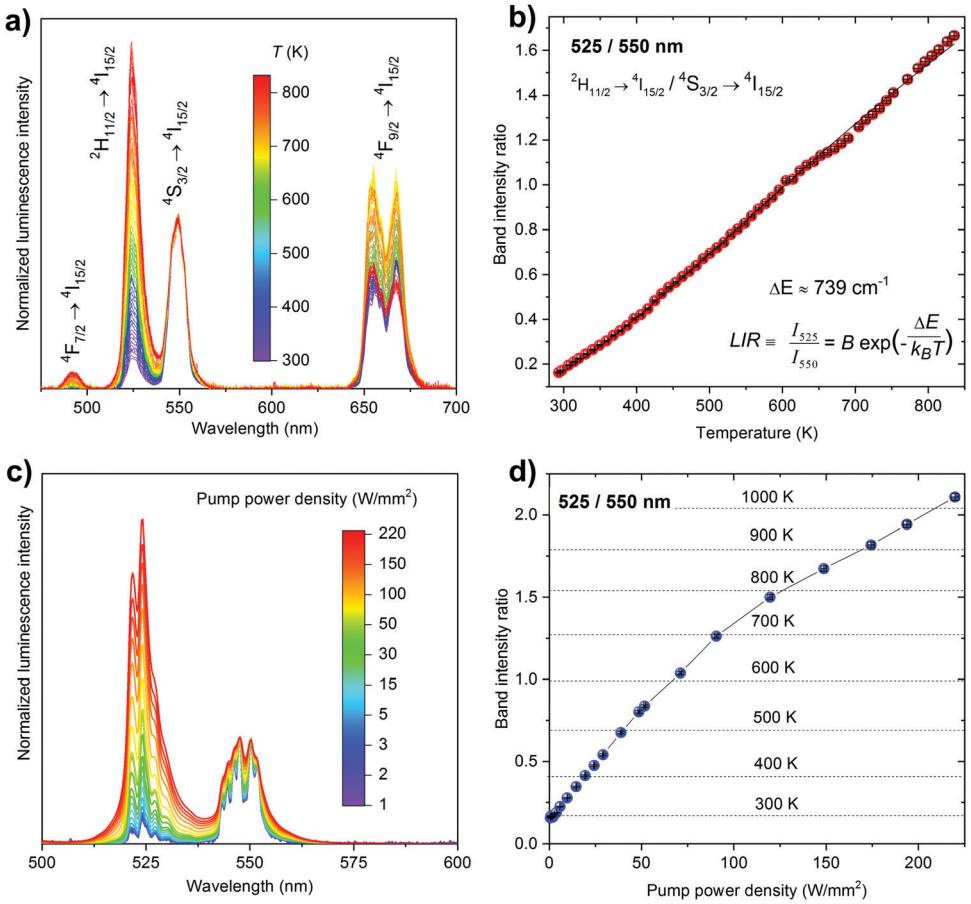


Fig. 1 UC emission as a function of temperature and pump power. (a) Normalized UC luminescence spectra of the $YPO_4$:$Yb^{3+}$–$Er^{3+}$ material as a function of temperature, measured at $\lambda_{ex}$ = 975 nm and ≈2 W mm$^{-2}$. (b) determined band intensity ratios, *i.e.*, $Er^{3+}$ LIR of 525/550 nm as a function of temperature. (c) Normalized UC emission spectra as a function of pump power. (d) Determined $Er^{3+}$ LIR of 525/550 nm as a function of pump power and the corresponding local temperature values (dashed lines) calculated using eqn (1).

distribution, so we could easily fit them with the following function:

$$\mathrm{LIR} \equiv \frac{I_{525}}{I_{550}} = B \exp\left(-\frac{\Delta E}{k_B T}\right) \quad (1)$$

where LIR is the band (luminescence) intensity ratio (525/550 nm); $\Delta E$ is the energy difference between the band centroids; $k_B$ is the Boltzmann constant; $T$ is the absolute temperature; and $B$ is a constant, which depends on the states degeneracies, branching ratio of the transitions in relation to the ground state, and rates of total spontaneous emission and energy of the transitions.[6] The fitting performed using eqn (1), resulted in the $\Delta E \approx 739 \pm 3$ cm$^{-1}$ (slightly lower compared to the value derived from the spectra, most plausibly due to band overlapping), $B \approx 5.81$ and $R^2 \approx 0.999$. This contactless, ratiometric method is commonly used in luminescence thermometry, ensuring good sensitivity, accuracy and repeatability of optical determination of the local temperature values. The detailed characteristics of the luminescent thermometer performance, including thermal cycling experiments, temperature sensitivity and resolution, as well as comparison with different optical thermometers from other reports are given in the ESI† (see Fig. S5–S7 and Table S1, respectively).

With the temperature response of the sensor in hand, in the next step we irradiated the sample with an increasing laser power (1–220 W mm$^{-2}$), to determine the light-to-heat conversion efficiency under ambient conditions. Similarly like in the case of heating experiments, the discussed band intensity ratio (LIR; 525/550 nm) of $Er^{3+}$ increases as a function of laser power (Fig. 1c and d), indicating the local temperature elevation, up to around 1000 K at ≈200 W mm$^{-2}$ (see Fig. 1d).

In the next step, we have recorded the UC emission spectra as a function of laser power (≈0.5–18 W mm$^{-2}$) under vacuum conditions (≈$10^{-5}$ bar). The band intensity ratio of 525/550 nm increases significantly at a much lower pump power (Fig. 2a), compared to the laser-heating experiments performed under ambient conditions. The heating rate, *i.e.*, the light-to-heat conversion efficiency is much higher under vacuum compared to ambient pressure (see Fig. 2b), resulting in the elevation of the local temperature up to ≈1000 K, at a laser power of <20 W mm$^{-2}$. This indicates more than 10-times enhancement of the light-to-heat conversion under vacuum conditions. The observed enhancement of local heating of the sample is associated with less efficient heat dissipation (convection) in vacuum, where the amount of air molecules is significantly limited. Whereas under

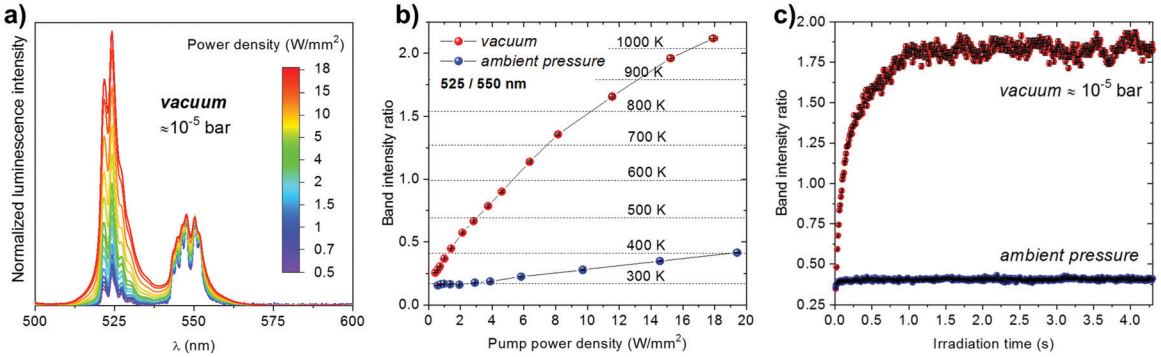


Fig. 2 UC luminescence under vacuum conditions. (a) Normalized UC emission spectra of the $YPO_4$:$Yb^{3+}$–$Er^{3+}$ material, measured as a function of pump power ($\lambda_{ex}$ = 975 nm) under vacuum conditions. (b) Comparison of the determined band intensity ratios, *i.e.*, $Er^{3+}$ LIR of 525/550 nm under vacuum (red) and at atmospheric pressure (blue), recorded as a function of pump power, and the corresponding local temperature values (dashed lines) calculated using eqn (1). (c) Temporal evolution of the determined LIR parameter as a function of irradiation time (≈15 W mm$^{-2}$), recorded under vacuum (red) and at atmospheric pressure (blue).

ambient pressure, abundant air molecules (cooling gas) transfer the generated heat into the surroundings. That is why, the determined LIR parameter (which is directly related to the local temperature of the sample) has much higher values in a vacuum, compared to the ambient pressure. Additionally, in Fig. 2c we present temporal evolution of the determined LIR parameter as a function of irradiation time, indicating stabilization of the local temperature after 1 s (top; red) and 0.1 s (bottom; blue) of laser irradiation (≈15 W mm$^{-2}$), under vacuum and ambient conditions, respectively. Longer stabilization time (equilibrium between the competing heating–cooling processes) under vacuum conditions is due to different heat dissipation mechanisms, as in the case of ambient pressure the dominant role in the cooling process is played by air molecules (convection process), whereas under vacuum conditions the slower process of heat conduction within the sample dominates. Nonetheless, the temporal resolution of this phosphate-based sensor is much better, compared to our previous vanadate-based vacuum sensor, which reaches equilibrium after about 5 s.[10]

Finally, in order to develop the luminescent low pressure sensor, we have measured a series of UC emission spectra at fixed laser power (≈15 W mm$^{-2}$) and different vacuum levels (see Fig. 3a). It is clear that the band intensity ratio (525/550 nm) associated with the discussed TCLs of $Er^{3+}$ significantly increases with the vacuum level of the system (1000–0.03 mbar), confirming the light-to-heat conversion enhancement under vacuum conditions. We have plotted the determined LIR parameter in Fig. 3b in the logarithmic representation, and using a simple linear fit

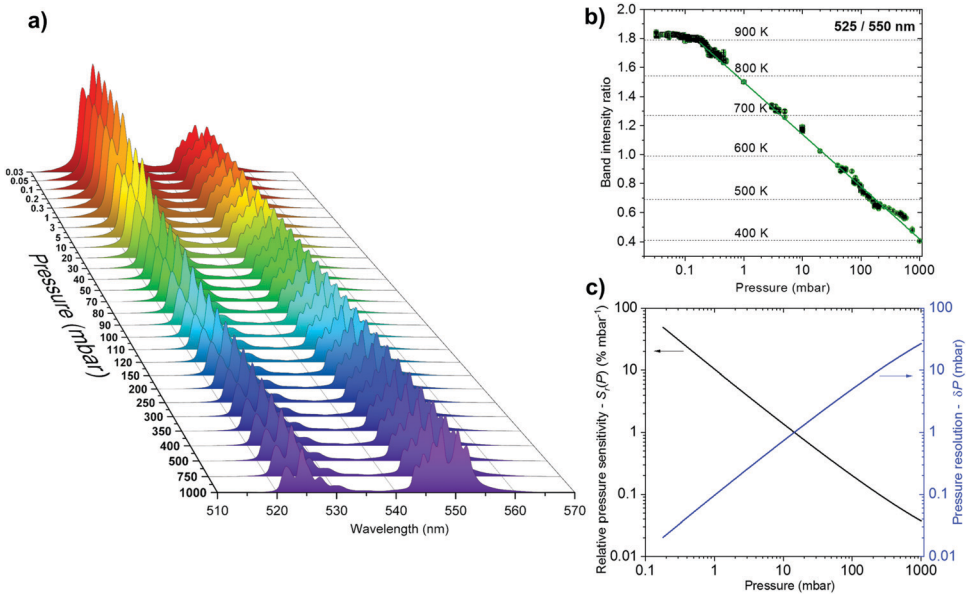


Fig. 3 Low-pressure, *i.e.*, vacuum, sensing. (a) Normalized UC emission spectra of the $YPO_4$:$Yb^{3+}$–$Er^{3+}$ material ($\lambda_{ex}$ = 975 nm; ≈15 W mm$^{-2}$), measured as a function of low-pressure, *i.e.*, vacuum. (b) Determined band intensity ratios, *i.e.*, $Er^{3+}$ LIR of 525/550 nm as a function of vacuum, and the corresponding local temperature values (dashed lines) calculated using eqn (1); the continuous line corresponds to the applied linear fit. (c) Relative pressure sensitivity, *i.e.*, $S_r(P)$, and pressure resolution, *i.e.*, $\delta P$, plotted as a function of vacuum.

 

(LIR = $-0.3601P + 1.4999$) we correlated the LIR values with the vacuum level of the system, from 0.2 to 1000 mbar ($R^2 = 0.99$). Most importantly, in contrast to the vanadate-based sensor (allowing sensing in a limited vacuum range, from $\approx 10^{-1}$ to $10^{1}$ mbar), the measured sensing parameter, *i.e.*, LIR, exhibits a significant and monotonic change over 4 orders of magnitude, *i.e.*, from $10^{-1}$ to $10^{3}$ mbar. This is the reason it also allows vacuum sensing close to the atmospheric pressure range, which is important from the point of view of science and industry. Fig. 3c presents the relative pressure sensitivity – $S_r(P)$ and resolution of pressure sensing – $\delta P$, determined based on the following equations:

$$S_r(P) = 100\% \times \frac{1}{\mathrm{LIR}} \frac{d\mathrm{LIR}}{dP} \quad (2)$$

and

$$\delta P = \frac{1}{S_r(P)} \frac{\delta \mathrm{LIR}}{\mathrm{LIR}} \quad (3)$$

where δLIR is the uncertainty of determination of the band intensity ratio (525/550 nm). The $S_r(P)$ decreases with pressure, from ≈50% mbar$^{-1}$ (at around 0.2 mbar), down to ≈0.04% mbar$^{-1}$ at atmospheric pressure. Whereas the pressure resolution, *i.e.*, $\delta P$ changes from 0.02 mbar to ≈27 mbar at ambient pressure, respectively. The obtained resolution is similar to the vanadate-based sensor, in the comparable pressure ranges.[10] Additionally, the reliability of our method is confirmed by cycling the sample between atmospheric pressure and vacuum, and the repetitive determination of the LIR parameter (the band intensity ratio 525/550 nm of $Er^{3+}$), which is fully reversible, as expected (see Fig. S8, ESI†).

### High pressure sensing

In order to optically monitor high pressure with our sensor, we have determined the spectral shift rate of one of the Stark sublevel of the $Er^{3+}$ emission band located in the NIR region, namely the $^4I_{13/2} \rightarrow {}^4I_{15/2}$ transition, centred at around 1550 nm ($\lambda_{ex}$ = 975 nm; 2 W mm$^{-2}$). This band ($^4I_{13/2} \rightarrow {}^4I_{15/2}$) splits into several crystal-field components (Stark sublevels), starting from ≈1500 nm and ending at ≈1600 nm. It is worth noting that in the case of high-pressure measurements we did not focus on the transitions located in the visible range, because they are

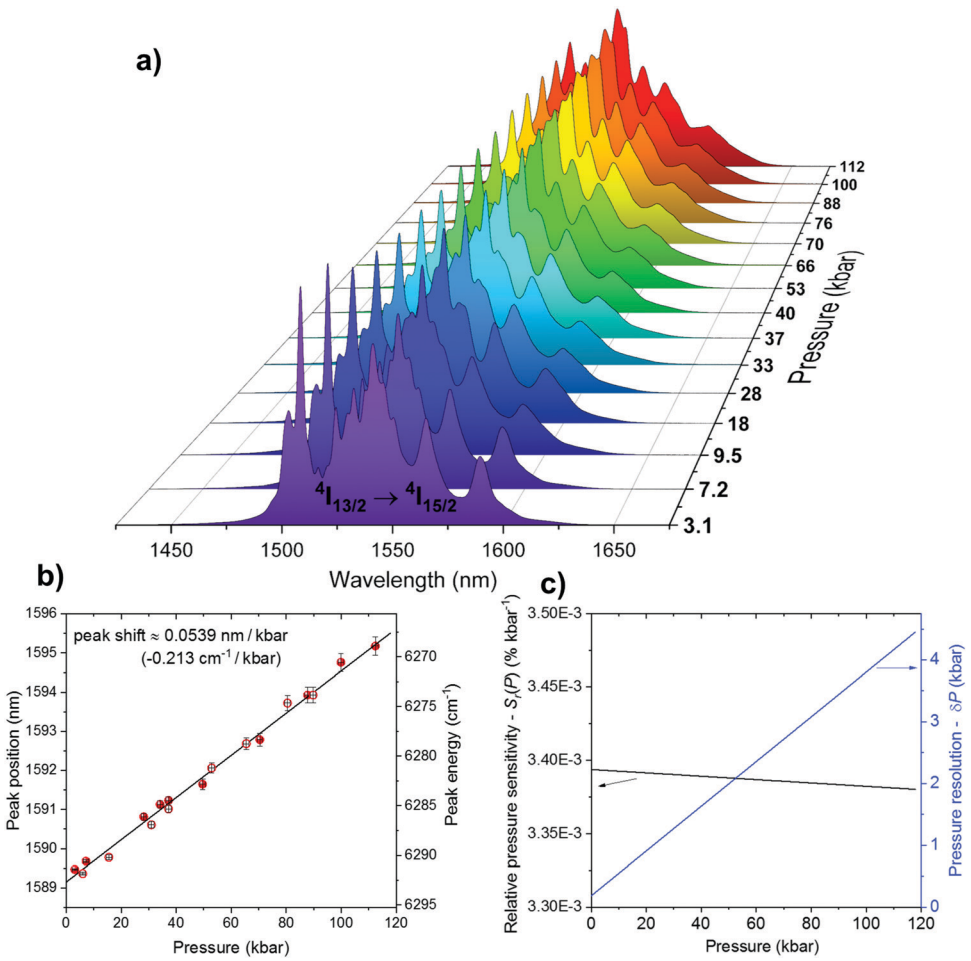


Fig. 4 High-pressure sensing. (a) Normalized NIR emission spectra of the $YPO_4$:$Yb^{3+}$–$Er^{3+}$ material ($\lambda_{ex}$ = 975 nm), measured as a function of high-pressure. (b) Determined spectral positions of the $^4I_{13/2} \rightarrow {}^4I_{15/2}$ band (Stark sublevel) of $Er^{3+}$ as a function of high-pressure; the continuous line corresponds to the applied linear fit; the filled symbols represent the compression and the empty ones decompression data. (c) Relative pressure sensitivity, *i.e.*, $S_r(P)$, and pressure resolution, *i.e.*, $\delta P$, plotted as a function of high-pressure.

generally less sensitive to pressure changes compared to the lower-energy transitions.[3–7] The emission spectra recorded as a function of high-pressure (up to 112 kbar, *i.e.*, ≈11 GPa) are presented in Fig. 4a. Due to the increasing crystal-field strength under high-pressure conditions, caused by the shortening of interionic distances ($Er^{3+}$–$O^{2-}$) and stronger interactions between the ions in the compressed crystal lattice, the splitting of the observed Stark sublevels is enhanced with increasing pressure.[5,7,26,40] That is why the left part of the band (Stark sublevels located at shorter wavelengths) exhibits a blue-shift, whereas the right part of the band (higher wavelengths) red-shifts.[3,5,7] This effect superimposes with the commonly reported decreasing energy difference between the ground and excited states of lanthanide ions (in this case $Er^{3+}$), leading to the red-shift of their emission bands under high-pressure conditions, which is related to the increased bonding covalency of the compressed material (enhanced nephelauxetic effect).[5,7,26,40] That is why, the Stark sublevel located at the longest wavelength shifts more, compared to the one located at the opposite side of that transition. Fig. 4b and Fig. S9–S11 (ESI†) present the determined spectral positions and the corresponding shift rates for the most intense Stark sublevels, namely 0.0539 nm $kbar^{-1}$ (at 1589 nm), 0.0199 nm $kbar^{-1}$ (at 1565 nm), −0.0459 nm $kbar^{-1}$ (at 1542 nm) and −0.0297 nm $kbar^{-1}$ (at 1508 nm), respectively. The observed spectral shifts are reversible, as confirmed by the decompression data. For the Stark sublevel exhibiting the greatest spectral shift and good linear fitting, with $R^2 \approx 0.99$ (see Fig. 4b), we have also determined the relative pressure sensitivity ($S_r(P)$) and pressure resolution, which are plotted as a function of pressure in Fig. 4c. Please note that to calculate the mentioned sensitivity and resolution values we have used the same equations as those for low-pressure sensing, *i.e.*, eqn (2) and (3), applying the determined spectral position of the emission line as a measured parameter (instead of LIR). Because the relative changes of the measured parameter, *i.e.*, line shifts are typically smaller compared to the LIR, the determined $S_r(P)$ values are small, being around $\approx 3.4 \times 10^{-3}$% $mbar^{-1}$ in the whole high-pressure range. However, most importantly, the resulting pressure resolution is quite good, *i.e.*, $\delta P \approx 2$ kbar at around 50 kbar, which is crucial for pressure sensing purposes.

Additionally, we have measured the emission spectra of $Er^{3+}$ in the same NIR spectral range, as a function of temperature,

Table 1 Comparison of low (vacuum) and high-pressure sensitivities of different luminescent manometers used for optical pressure sensing

Low-pressure (vacuum) sensors

| Host | Emitting ion | Sensitivity $S_r(P)$ (% $mbar^{-1}$) | Resolution $\delta P$ (mbar) | Transitions | $\lambda$ (nm) | Ref. |
|---|---|---|---|---|---|---|
| $YPO_4$ | $Er^{3+}$ | 10 (at 1 mbar)<br>1 (at 10 mbar) | 0.1 (at 1 mbar)<br>1 (at 10 mbar) | $^2H_{11/2} \rightarrow {}^4I_{15/2}/{}^4S_{3/2} \rightarrow {}^4I_{15/2}$ | 525/550 | This work |
| $YVO_4$ | $Er^{3+}$ | 40 (at 1 mbar)<br>1 (at 10 mbar) | 0.025 (at 1 mbar)<br>1 (at 10 mbar) | $^2H_{11/2} \rightarrow {}^4I_{15/2}/{}^4S_{3/2} \rightarrow {}^4I_{15/2}$ | 525/550 | 10 |
| $YAlO_3$ (microsphere) | $Nd^{3+}$ | <0.1 (at 1 mbar) | 0.015 (at 1 mbar) | $^4F_{3/2} \rightarrow {}^4I_{9/2}$ | 914 | 11 |
| PtTFPL | Organic complex | ∼0.1 | — | Triplet–singlet | 740 | 41 |
| PtTFPP | | ∼0.1 | — | | 650 | 42 |

High-pressure sensors

| Host | Emitting ion | Sensitivity – line shift (nm $kbar^{-1}$) | T-shift (nm $K^{-1}$) | Transitions | $\lambda$ (nm) | Ref. |
|---|---|---|---|---|---|---|
| $YPO_4$ | $Er^{3+}$ | 0.0539 | $-1.78 \times 10^{-3}$ | $^4I_{13/2} \rightarrow {}^4I_{15/2}$ (Stark) | 1589 | This work |
| $Al_2O_3$ (ruby) | $Cr^{3+}$ | 0.0365 | $6.8 \times 10^{-3}$ | $^2E \rightarrow {}^4A_2$ | 694 | 27 |
| $YAlO_3$ | $Cr^{3+}$ | 0.070 | $7.6 \times 10^{-3}$ | $^2E \rightarrow {}^4A_2$ | 723 | 43 |
| $YF_3$ | $Er^{3+}$ | 0.01855 | $-3 \times 10^{-4}$ | $^4F_{9/2} \rightarrow {}^4I_{15/2}$ (Stark) | 665 | 4 |
| $NaBiF_4$ | $Er^{3+}$ | −0.08 | — | $^4I_{13/2} \rightarrow {}^4I_{15/2}$ (Stark) | 1503 | 3 |
| $YAlO_3$ | $Nd^{3+}$ | −0.013 | $1 \times 10^{-6}$ | $^4F_{3/2} \rightarrow {}^4I_{9/2}$ (Stark) | 875 | 43 |
| $Gd_3Sc_2Ga_3O_{12}$ | $Nd^{3+}$ | ∼0.0632 | — | $^4F_{3/2} \rightarrow {}^4I_{9/2}$ (Stark) | 935 | 44 |
| $Y_3Al_5O_{12}$ | $Eu^{3+}$ | 0.0197 | $-5.4 \times 10^{-4}$ | $^5D_0 \rightarrow {}^7F_1$ | 591 | 45 |
| $EuPO_4$ | $Eu^{3+}$ | ∼0.027 | — | $^5D_0 \rightarrow {}^7F_0$ | 580 | 46 |
| $Y_3Al_5O_{12}$ | $Sm^{3+}$ | 0.030 | $2.3 \times 10^{-4}$ | $^4G_{5/2} \rightarrow {}^6H_{7/2}$ (Stark) | 618 | 47 |
| SrFCl | $Sm^{2+}$ | 0.110 | $-2.3 \times 10^{-3}$ | $^5D_0 \rightarrow {}^7F_0$ | 690 | 48 |
| $SrB_4O_7$ | $Sm^{2+}$ | 0.0255 | $-1 \times 10^{-4}$ | $^5D_0 \rightarrow {}^7F_0$ | 685 | 49 |
| $SrB_2O_4$ | $Sm^{2+}$ | 0.0244 | $-1 \times 10^{-4}$ | $^5D_0 \rightarrow {}^7F_0$ | 685 | 25 |
| $BaLi_2Al_2Si_2N_6$ | $Eu^{2+}$ | 0.158 | — | 5d → 4f | 532 | 26 |
| $KMgF_3$ | $Eu^{2+}$ | ∼0.013 | — | 5d → 4f | 360 | 50 |
| CeN–PVDF | $Ce^{3+}$ | 0.028 | — | 5d → 4f | 327 | 51 |
| CeS–PVDF | $Ce^{3+}$ | 0.01 | — | 5d → 4f | 340 | 51 |
| $LaPO_4$ | $Tm^{3+}$ | 0.01 | $-2 \times 10^{-3}$ | $^1G_4 \rightarrow {}^3H_6$ | 475 | 7 |
| | | 0.8% (band ratio) | — | $^3H_4 \rightarrow {}^3H_6/{}^1G_4 \rightarrow {}^3H_6$ | 800/475 | |
| $Y_6Ba_4(SiO_4)_6F_2$ | $Ce^{3+}$ | 0.063 | — | $^2D_J \rightarrow {}^2F_J$ (5d → 4f) emission | 466 | 52 |
| | | 0.15% (FWHM) | | $^2F_J \rightarrow {}^2D_J$ (4f → 5d) excitation | 342 | |
| | | 0.25% (FWHM) | | | | |
| $SrF_2$ | $Er^{3+}$ | 0.77% | — | $^4F_{9/2} \rightarrow {}^4I_{15/2}$ | 653 | 53 |
| | | 0.64% | | $^4S_{3/2} \rightarrow {}^4I_{15/2}$ | 538 | |
| | | 0.62% (lifetimes) | | $^2H_{11/2} \rightarrow {}^4I_{15/2}$ | 516 | |

 

and determined the spectral positions of the Stark sublevels of $Er^{3+}$ ($^4I_{13/2} \rightarrow {}^4I_{15/2}$ transition), in order to verify the potential temperature drift/correction for the sensor (see Fig. S12 and S13, ESI†). Fortunately, up to ≈500 K, there is almost no change in the spectral position of the measured bands (Fig. S13, ESI†), which is typical of lanthanide ($Ln^{3+}$) emission.[6] This result is of great importance from the point-of-view of the researchers/engineers performing the experiments, simultaneously under high-pressure/high-temperature conditions.[4]

Finally, we have compared in Table 1 the performance of the developed luminescent pressure sensor with the available literature data. Please note, that for the vacuum sensors we compared the relative sensitivity and resolution, but for the high-pressure sensors we mainly used the line shift and the corresponding temperature correction. This is because most of the high-pressure sensors are based on the emission line shift, hence there are no literature data available about their relative sensitivity and resolution. In the case of luminescent vacuum sensors operating in the very low pressure range, *i.e.*, from about 0.1 mbar, the data are very limited. Depending on the pressure range of interest, the sensitivity of the developed sensor varies significantly, *i.e.*, at a pressure of around 1 mbar, $S_r(P) \approx 10\%\ mbar^{-1}$, which is lower compared to the vanadate-based sensor, but higher compared to the perovskite-based sensor (microsphere). However, at a pressure of around 10 mbar, $S_r(P) \approx 1\%\ mbar^{-1}$, which is the same for the vanadate sensor (perovskite sensor do no operate in this range). Resolution of the developed sensor also depends on the pressure range, however, at pressure around 10 mbar (*i.e.*, in the middle of the operating pressure range) it is the same for the developed phosphate sensor and for the already reported vanadate sensor, *i.e.*, $\delta P \approx 1$ mbar. Whereas comparing the performance of the high-pressure sensors, our material exhibits one of the largest spectral shift, *i.e.*, 0.0539 nm $kbar^{-1}$, which is much larger than that of the commonly used ruby-based sensor. Nonetheless, it is worth noting that this is the first time that a single optically active material is used for sensing in an unprecedentedly broad pressure range, encompassing vacuum and high-pressure regions.

## Conclusions

In this work, we have shown for the first time the possibility of optical sensing of low and high pressure values, utilizing a single, lanthanide-doped upconverting material. The active material used for sensing is based on the $YPO_4$:$Yb^{3+}$–$Er^{3+}$ luminophore, exhibiting UC luminescence in the visible range and down-shifting emission of $Er^{3+}$ in the NIR range, observed under 975 nm excitation. The sensing concept in the vacuum range is based on the laser-induced heating of the upconverting material, enhanced under vacuum conditions, and the use of $Er^{3+}$ band intensity ratio (525/550 nm) as a pressure-dependent sensing parameter. Whereas for sensing in the high-pressure range we used the spectral shift of the $Er^{3+}$ emission line (around 1590 nm), observed during materials compression in a diamond anvil cell (DAC). The developed sensing methods provide good pressure resolution, both in a vacuum and in the high-pressure ranges (uncertainty of about ≈3–4% of the measured pressure value), ensuring accurate pressure determination in the unprecedentedly broad pressure range, *i.e.*, from ≈$10^{-4}$ to $10^5$ bar. Another very important advantage of the presented luminescence manometry technique is its non-invasive character (optical detection), allowing pressure sensing in various environments.

## Experimental section

The starting materials $Y_2O_3$, $Yb_2O_3$, and $Er_2O_3$ (Alfa Aesar, 99.99%) were dissolved in excess chloric acid (Sigma-Aldrich, ASC 37%). The solutions were evaporated 3-times to dispose of HCl. The obtained $YCl_3$, $YbCl_3$, and $ErCl_3$ solutions were diluted with deionized water, and 0.5 M solutions were prepared. 0.198 g (25% excess) of $(NH_4)H_2PO_4$ (Sigma-Aldrich, ACS, >98%) was dissolved in 30 ml of glycerol (POCH, >99.5%) and 90 ml of deionized water. The prepared solution was mixed at 323 K for 30 min. Next, a stoichiometric amount (calculated on the basis of the formula $Y_{1-x-y}Yb_xEr_yPO_4$ where $x = 0.15$; $y = 0.02$) of $YCl_3$, $YbCl_3$ and $ErCl_3$ solutions were added dropwise. White material starts to precipitate at the time of mixing. Finally, the prepared solution was stirred continuously at 323 K for 30 min. The synthesized material was collected by centrifugation and washed with water five times. The obtained material was dried at 353 K for 24 h in air, and then ground in an agate mortar. Next, the sample was annealed at 1273 K for 2 h. The elemental composition, *i.e.*, chemical formula of the synthesized material, determined by the energy-dispersive X-ray (EDX) analysis is found to be $YPO_4$:16 mol% $Yb^{3+}$,2.7 mol% $Er^{3+}$.

### Characterization

Scanning electron microscopy (SEM) and EDX analyses were performed using a Scanning Electron Microscope FEI Quanta 250 FEG, and an EDAX detector. The Powder X-ray diffraction (XRD) pattern was recorded with a Bruker AXS D8 Advance diffractometer, using Cu Kα1 radiation ($\lambda$ = 0.15406 nm). The FT-IR spectrum was measured in a KBr pellet (transmission mode) using a FT-IR spectrophotometer JASCO 4200. UC emission spectra in the visible range and the emission spectra in the NIR range were recorded using an Andor Shamrock 500 spectrometer, coupled to the silicon (visible range detection) and InGaAs (NIR range detection) CCD cameras from Andor. The excitation source was a tunable CW Ti:Sapphire laser system, Spectra Physics 3900-S pumped with a 15 W 532 nm Spectra Physics Millenia, adjusted at 975 nm. The procedures of luminescence measurements in a vacuum chamber and under high-pressure conditions (in a DAC) are described in detail in our previous publications.[4,7,10]

### DAC loading procedure and high-pressure detection

High-pressure measurements were carried out in a DAC (400 μm culet size) made at Universität Paderborn (Germany), where the pressure is adjusted by the use of four metal screws. Stainless

steel sheets (200 μm thick) were used as gaskets. The gaskets were pre-indented down to ~50 μm thickness, and then drilled with an electro-driller, to form a hole of ~100 μm diameter. After mounting the metal gasket on the diamond cell, a small sphere of ruby and the sample (white powder) were placed in the gasket hole, and filled with a methanol : ethanol : water (16 : 3 : 1) pressure transmitting medium (hydrostatic up to ~10 GPa). The high-pressure values were determined using the $R_1$ ruby florescence line shift, excited by a 532 nm laser, and using a ruby calibration curve available elsewhere.[54]

### Low-pressure (vacuum) measurements

Luminescence measurements in a low-pressure range were performed for the material (~100 μm thick) placed on a small glass plate, in the centre of the vacuum chamber. The low-pressure values were monitored using a digital vacuum sensor. For all experiments, the material was used in the form of a fine powder. More technical details can be found in ref. 10.

## Conflicts of interest

The authors declare no competing financial interest.

## Acknowledgements

This work was supported by the Polish National Science Centre, grant no. 2016/23/D/ST4/00296 and 2018/31/N/ST5/00636, the Ministerio de Economía y Competitividad (MINECO) under the Spanish National Program of Materials (PID2019-106383GB-C44 and PID2019-107335RA-I00), the Gobierno de Canarias (ProID2020010067), the EU-FEDER funds, and by the grant no. POWR.03.02.00-00-I023/17 co-financed by the European Union through the European Social Fund under the Operational Program Knowledge Education Development. M. R. is a recipient of the Bekker Programme scholarship supported by the Polish National Agency for Academic Exchange.

## References

1 Y. Fei and Y. Wang, *Rev. Mineral. Geochem.*, 2000, **41**, 521–557.
2 *An Introduction to High-Pressure Science and Technology*, ed. J. M. Recio, J. M. Menendez and A. Otero de la Roza, CRC Press, Boca Raton, 2016.
3 M. A. Antoniak, S. J. Zelewski, R. Oliva, A. Żak, R. Kudrawiec and M. Nyk, *ACS Appl. Nano Mater.*, 2020, **3**, 4209–4217.
4 S. Goderski, M. Runowski, P. Woźny, V. Lavín and S. Lis, *ACS Appl. Mater. Interfaces*, 2020, **12**, 40475–40485.
5 T. Tröster, in *Handbook on the Physics and Chemistry of Rare Earths*, ed. K. A. Gschneidner, J.-C. G. Bünzli and V. K. Pecharsky, Elsevier, North-Holland, 2003, vol. 33, pp. 515–589.
6 C. D. S. Brites, A. Millán and L. D. Carlos, *Handbook on the Physics and Chemistry of Rare Earths*, 2016, vol. 49, pp. 339–427.
7 M. Runowski, A. Shyichuk, A. Tymiński, T. Grzyb, V. Lavín and S. Lis, *ACS Appl. Mater. Interfaces*, 2018, **10**, 17269–17279.
8 K. Dziubek, M. Citroni, S. Fanetti, A. B. Cairns and R. Bini, *J. Phys. Chem. C*, 2017, **121**, 2380–2387.
9 A. Katrusiak, *Acta Crystallogr., Sect. B: Struct. Sci., Cryst. Eng. Mater.*, 2019, **75**, 918–926.
10 M. Runowski, P. Woźny, S. Lis, V. Lavín and I. R. Martín, *Adv. Mater. Technol.*, 2020, **5**, 1901091.
11 K. Soler-Carracedo, I. R. Martin, M. Runowski, L. L. Martín, F. Lahoz, A. D. Lozano-Gorrín and F. Paz-Buclatin, *Adv. Opt. Mater.*, 2020, **8**, 2000678.
12 D. Jaque and F. Vetrone, *Nanoscale*, 2012, **4**, 4301–4326.
13 M. D. Dramićanin, *J. Appl. Phys.*, 2020, **128**, 040902.
14 P. Shi, Y. Duan, W. Wei, Z. Xu, Z. Li and T. Han, *J. Mater. Chem. C*, 2018, **6**, 2476–2482.
15 J. C. G. Bünzli and C. Piguet, *Chem. Soc. Rev.*, 2005, **34**, 1048–1077.
16 M. Sato, S. W. Kim, Y. Shimomura, T. Hasegawa, K. Toda and G. Adachi, in *Handbook on the Physics and Chemistry of Rare Earths*, ed. J.-C. G. Bunzli and V. K. Pecharsky, Elsevier, 2016, p. 16.
17 J.-C. G. Bünzli, *Trends Chem.*, 2019, **1**, 751–762.
18 B. Golesorkhi, H. Nozary, A. Fürstenberg and C. Piguet, *Mater. Horiz.*, 2020, **7**, 1279–1296.
19 R. G. Geitenbeek, H. W. De Wijn and A. Meijerink, *Phys. Rev. Appl.*, 2018, **10**, 1.
20 P. Du, L. Luo, H.-K. Park and J. S. Yu, *Chem. Eng. J.*, 2016, **306**, 840–848.
21 P. Du, L. Luo, W. Li, Q. Yue and H. Chen, *Appl. Phys. Lett.*, 2014, **104**, 152902.
22 M. Runowski, P. Woźny, N. Stopikowska, I. R. Martín, V. Lavín and S. Lis, *ACS Appl. Mater. Interfaces*, 2020, **12**, 43933–43941.
23 S. V. Rashchenko, A. Kurnosov, L. Dubrovinsky and K. D. Litasov, *J. Appl. Phys.*, 2015, **117**, 2–7.
24 T. Zheng, M. Runowski, P. Woźny, S. Lis and V. Lavín, *J. Mater. Chem. C*, 2020, **8**, 4810–4817.
25 M. Runowski, P. Woźny, V. Lavín and S. Lis, *Sens. Actuators, B*, 2018, **273**, 585–591.
26 Y. Wang, T. Seto, K. Ishigaki, Y. Uwatoko, G. Xiao, B. Zou, G. Li, Z. Tang, Z. Li and Y. Wang, *Adv. Funct. Mater.*, 2020, **30**, 2001384.
27 H. K. Mao, J. Xu and P. M. Bell, *J. Geophys. Res.*, 1986, **91**, 4673–4676.
28 A. Dewaele, M. Torrent, P. Loubeyre and M. Mezouar, *Phys. Rev. B: Condens. Matter Mater. Phys.*, 2008, **78**, 104102.
29 F. Datchi, A. Dewaele, P. Loubeyre, R. Letoullec, Y. Le Godec and B. Canny, *High Pressure Res.*, 2007, **27**, 447–463.
30 J. W. Gregory, K. Asai, M. Kameda, T. Liu and J. P. Sullivan, *Proc. Inst. Mech. Eng., Part G*, 2008, **222**, 249–290.
31 S. M. Peak and A. N. Watkins, *ACS Appl. Nano Mater.*, 2020, **3**, 9813–9821.
32 P. Cortelletti, A. Skripka, C. Facciotti, M. Pedroni, G. Caputo, N. Pinna, M. Quintanilla, A. Benayas, F. Vetrone and A. Speghini, *Nanoscale*, 2018, **10**, 2568–2576.

 

33 *Near Infrared-Emitting Nanoparticles for Biomedical Applications*, ed. A. Benayas, E. Hemmer, G. Hong and D. Jaque, Springer, Cham, 2020.
34 C. D. S. Brites, K. Fiaczyk, J. F. C. B. Ramalho, M. Sójka, L. D. Carlos and E. Zych, *Adv. Opt. Mater.*, 2018, **6**, 1701318.
35 S. Balabhadra, M. L. Debasu, C. D. S. Brites, R. A. S. Ferreira and L. D. Carlos, *J. Phys. Chem. C*, 2017, **121**, 13962–13968.
36 M. Runowski, in *Handbook of Nanomaterials in Analytical Chemistry*, ed. C. M. Hussain, Elsevier, 2020, pp. 227–273.
37 K. Trejgis, A. Bednarkiewicz and L. Marciniak, *Nanoscale*, 2020, **12**, 4667–4675.
38 L. Marciniak, K. Elzbieciak-Piecka, K. Kniec and A. Bednarkiewicz, *Chem. Eng. J.*, 2020, **388**, 124347.
39 F. X. Zhang, J. W. Wang, M. Lang, J. M. Zhang, R. C. Ewing and L. A. Boatner, *Phys. Rev. B: Condens. Matter Mater. Phys.*, 2009, **80**, 184114.
40 ed. K. L. Bray, M. Glasbeek, H. Kunkely, A. Vogler and H. Yersin, *Transition Metal and Rare Earth Compounds Excited States, Transitions, Interactions I*, New York, Springer, 2001.
41 B. Zelelow, G. E. Khalil, G. Phelan, B. Carlson, M. Gouterman, J. B. Callis and L. R. Dalton, *Sens. Actuators, B*, 2003, **96**, 304–314.
42 J. W. Gregory, H. Sakaue, T. Liu and J. P. Sullivan, *Annu. Rev. Fluid Mech.*, 2014, **46**, 303–330.
43 J. D. Barnett, S. Block and G. J. Piermarini, *Rev. Sci. Instrum.*, 1973, **44**, 1–9.
44 S. F. León-Luis, J. E. Muñoz-Santiuste, V. Lavín and U. R. Rodríguez-Mendoza, *Opt. Express*, 2012, **20**, 10393.
45 H. Arashi and M. Ishigame, *Jpn. J. Appl. Phys.*, 1982, **21**, 1647–1649.
46 G. Chen, J. Hölsä and J. R. Peterson, *J. Phys. Chem. Solids*, 1997, **58**, 2031–2037.
47 N. J. Hess and G. J. Exarhos, *High Pressure Res.*, 1989, **2**, 57–64.
48 Y. R. Shen and W. B. Holzapfel, *Phys. Rev. B: Condens. Matter Mater. Phys.*, 1995, **51**, 15752–15762.
49 F. Datchi, R. LeToullec and P. Loubeyre, *J. Appl. Phys.*, 1997, **81**, 3333–3339.
50 J. Barzowska, T. Lesniewski, S. Mahlik, H. J. Seo and M. Grinberg, *Opt. Mater.*, 2018, **84**, 99–102.
51 C. Hernandez, S. K. Gupta, J. P. Zuniga, J. Vidal, R. Galvan, M. Martinez, H. Guzman, L. Chavez, Y. Mao and K. Lozano, *Sens. Actuators, A*, 2019, **298**, 111595.
52 M. Runowski, P. Woźny, N. Stopikowska, Q. Guo and S. Lis, *ACS Appl. Mater. Interfaces*, 2019, **11**, 4131–4138.
53 M. Runowski, J. Marciniak, T. Grzyb, D. Przybylska, A. Shyichuk, B. Barszcz, A. Katrusiak and S. Lis, *Nanoscale*, 2017, **9**, 16030–16037.
54 K. Syassen, *High Pressure Res.*, 2008, **28**, 75–126.